Interhemispheric antiphasing of neotropical precipitation during the past millennium

Byron A. Steinman[a,b,1], Nathan D. Stansell[c], Michael E. Mann[d,1], Colin A. Cooke[e] [ID], Mark B. Abbott[f] [ID], Mathias Vuille[g] [ID], Broxton W. Bird[h] [ID], Matthew S. Lachniet[i] [ID], and Alejandro Fernandez[a,b]

Uncertainty about the influence of anthropogenic radiative forcing on the position and strength of convective rainfall in the Intertropical Convergence Zone (ITCZ) inhibits our ability to project future tropical hydroclimate change in a warmer world. Paleoclimatic and modeling data inform on the timescales and mechanisms of ITCZ variability; yet a comprehensive, long-term perspective remains elusive. Here, we quantify the evolution of neotropical hydroclimate over the preindustrial past millennium (850 to 1850 CE) using a synthesis of 48 paleo-records, accounting for uncertainties in paleo-archive age models. We show that an interhemispheric pattern of precipitation antiphasing occurred on multicentury timescales in response to changes in natural radiative forcing. The conventionally defined "Little Ice Age" (1450 to 1850 CE) was marked by a clear shift toward wetter conditions in the southern neotropics and a less distinct and spatio-temporally complex transition toward drier conditions in the northern neotropics. This pattern of hydroclimatic change is consistent with results from climate model simulations indicating that a relative cooling of the Northern Hemisphere caused a southward shift in the thermal equator across the Atlantic basin and a southerly displacement of the ITCZ in the tropical Americas, with volcanic forcing as the principal driver. These findings are at odds with proxy-based reconstructions of ITCZ behavior in the western Pacific basin, where changes in ITCZ width and intensity, rather than mean position, appear to have driven hydroclimate transitions over the last millennium. This reinforces the idea that ITCZ responses to external forcing are region specific, complicating projections of the tropical precipitation response to global warming.

paleoclimate | Intertropical Convergence Zone | neotropics | hydroclimate | last millennium

Although the climate of tropical Central and South America is relatively wet, the precipitation is highly seasonal and leads to an extended dry season in much of the region. Trends in observational data spanning the past ~50 y (see Fig. 1*A*, see *Materials and Methods*), for example, indicate precipitation reductions in Central America (e.g., the Dry Corridor) and eastern Brazil that recently have contributed to crop failures, malnourishment, and the migration of thousands of people (1, 2). These changes in neotropical hydroclimate could be a result of anthropogenic influences on the Intertropical Convergence Zone (ITCZ) (3), although this has yet to be conclusively determined.

In the tropical Americas, climate variability is dominated by seasonal variations of the North and South American Monsoon (NAM/SAM) systems and the latitudinal migration of the ITCZ, which control the timing and intensity of wet-season precipitation (4) (see Fig. 1*B*) through interactions with sea surface temperature (SST) and atmospheric circulation in the Atlantic and Pacific basins (*SI Appendix*). Over land, monsoonal convection arises from land mass heating, moisture convergence related to ITCZ position, and the interaction of moisture transport with local topography. As the upward branch of the convergent Hadley Cells, the ITCZ influences heat redistribution to higher latitudes and impacts hydroclimate globally (5).

While fundamentally linked, the ITCZ and monsoons are distinct systems (6). In South America, the SAM displays significant interannual- and decadal-scale variability in its intensity; yet the location of maximum precipitation is not easily displaced latitudinally because of orographic constraints (7). The position of the ITCZ, on the other hand, traverses ~7° of latitude on a seasonal basis over the central Atlantic and Pacific Oceans (8), achieving its northernmost extent during the boreal summer and vice versa in winter. Because the ITCZ contributes to convective activity over the SAM region, a southward displacement of its mean position can enhance both the moisture flux onto the continent and convective activity over the Amazon basin and downstream regions including the Andes, while a northward shift can enhance convection and moisture delivery over Central American and circum-Caribbean locations (7). The mean position

Significance

Understanding Intertropical Convergence Zone (ITCZ) responses to external forcing is critical for predicting climate change in a warming world. We analyzed paleoclimate records of precipitation change in the neotropics and climate model simulations that span the preindustrial last millennium to assess ITCZ behavior on multicentury timescales. Our results demonstrate that the ITCZ shifted southward during the Little Ice Age in the Atlantic basin in response to relative cooling of the Northern Hemisphere driven by volcanic forcing. This finding contrasts with studies suggesting that changes in ITCZ width and/or strength, rather than a change in mean position, occurred during the Little Ice Age. This reinforces the idea that ITCZ responses to external forcing are region specific.

Fig. 1. Observed precipitation trends and vertical atmospheric motion. (*A*) Trend (mm/y) in annual precipitation from 1970 to 2016 CE. Regions of significance (*P* ≤ 0.1) are marked by black dots. Precipitation data are the mean of three products (see *Materials and Methods*). (*B*) Vertical atmospheric motion (Omega) monthly mean (June minus January) (Pascal/s) from National Centers for Environmental Prediction/National Center for Atmospheric Research Reanalysis 1 (1981 to 2010 CE). The seasonal shift in ITCZ position and development of summer monsoons produce opposite responses in each hemisphere. Negative values represent upward vertical atmospheric movement. Paleoclimate record locations: circles, lake sediment; diamonds, speleothems; asterisks, ice; and squares, ocean sediment. Numbers correspond to *SI Appendix*, Table S1. Yellow locations are part of the Core region group.

of the ITCZ is thus a strong control on the monsoons, with increasing moisture availability and convection occurring in the hemisphere toward which the ITCZ shifts and vice versa, leading to an interhemispheric, antiphased precipitation response (8).

The latitudinal mean position of the ITCZ is governed by interhemispheric contrasts in temperature and upper atmosphere net radiative fluxes, wherein relative warming of either hemisphere produces anomalous cross-equatorial energy flow into the cooling hemisphere and a shift in the ITCZ toward the warming hemisphere (3). Studies that used idealized simulations with a "slab" ocean demonstrate that the ITCZ is located at the latitude where poleward atmospheric energy flux is zero (i.e., the "Energetic Theory") (9, 10), while more recent modeling studies accounting for tropical atmospheric dynamics suggest that ITCZ position is effectively offset equatorward of the maximum in SST (i.e., the "Dynamical Theory") (11). Both theories indicate that interhemispheric disparity in ocean temperature changes should latitudinally shift the mean position of the ITCZ. The Atlantic meridional SST gradient is thus a strong control on ITCZ position, with ITCZ displacement toward the hemisphere undergoing relative warming. In the

Pacific basin, ITCZ position is strongly influenced by both meridional and zonal SST gradients, with relative warming of the eastern tropical Pacific (e.g., during El Niño events) leading to a southward shift of the ITCZ.

One prevalent hypothesis asserts that the ITCZ mean position shifts northward on a global scale in response to greater hemispherically symmetric radiative forcing (and vice versa), owing to the Northern Hemisphere's relatively larger land mass (which has less thermal inertia than the ocean) and thus stronger response to radiative forcing (12). Consistent with this hypothesis, numerous studies based on paleoclimate archives have asserted that in the neotropics wetter conditions occurred in the south and drier conditions in the north during the Little Ice Age (LIA; 1450 to 1850 CE) (13), largely in response to a southward shift in ITCZ mean position. For example, hydroclimate records from northern South America (8), the Caribbean (14, 15), and Central America (16, 17) indicate drier conditions during the LIA, while numerous records from the Andes (7) reveal wetter conditions at this time. Paleo-data from the tropical Pacific (18) support the inferred southward shift in the ITCZ during the LIA, and a synthesis of paleo-records (19) suggests it was global in scale.

However, recent proxy-, observational-, and modeling-based studies have challenged the mean position shift hypothesis, suggesting instead that ITCZ responses to external forcing are likely region specific and more strongly characterized by changes in its width and/or strength. For example, Campos et al. (20) and Asmerom et al. (21) suggest that the ITCZ became wider and perhaps weaker in the neotropics during the LIA, and Yan et al. (22) and Griffiths et al. (23) show that the ITCZ did not shift southward in the western Pacific during the LIA but rather retracted equatorward (i.e., became narrower), while Scroxton et al. (24) show that similar precipitation changes occurred on both sides of the equator in the western Indian basin during the last millennium. The mean position shift hypothesis also does not appear to explain trends observed over the satellite era (1979 to present), during which the ITCZ has instead strengthened, become more narrow, and exhibited only a slight and statistically insignificant northward shift (3). Furthermore, model projections of changes in ITCZ position in response to anthropogenic forcing demonstrate indicate zonal heterogeneity, with different projected shifts in the neotropics and Asia (25), while simulations of the ITCZ during the last glacial maximum and mid-Holocene in Africa point to mean position, width, and strength changes as each being valid possibilities and not mutually exclusive for explaining ITCZ behavior under different boundary conditions (26). The diversity of conclusions from these studies demonstrates a lack of consensus on ITCZ dynamical responses to external forcing and indicate that further study of hydroclimate changes in the tropics is needed for a more robust characterization of the underlying mechanisms controlling tropical precipitation on multidecadal and longer timescales.

Here, we contribute to this debate by exploring the patterns and driving mechanisms of hydroclimate change in the neotropics over the preindustrial last millennium (850 to 1850 CE) through a comprehensive synthesis that incorporates 48 paleo-proxy records (see *Materials and Methods* for the selection process) and an analysis of a large ensemble of climate model simulations. A key advance is that our study synthesizes broadly distributed datasets based on a range of proxies (instead of individual or small groups of records); thus, it has the advantage of emphasizing the regional signal over the site-to-site and within-site noise arising from local climatic variability and inherent

proxy uncertainties. Our results reveal that a southerly shift in the ITCZ is likely to have occurred in the tropical Americas during the LIA, noting, however, that marked heterogeneity in the northern records cannot be explained solely through a shift in ITCZ mean position. Analysis of coupled climate model "last millennium" simulations demonstrates spatiotemporal precipitation and SST patterns that are largely consistent with the paleoclimate data and that point toward changes in the Atlantic meridional SST gradient as a principal control on neotropical precipitation variability on multicentury timescales. The simulations further indicate that volcanic rather than solar forcing appears to have been the main driver of these changes during the last millennium.

Results and Discussion

Paleoclimate Record Analysis. We compiled tropical American hydroclimate records from sites in Central America, the Caribbean, and South America distributed from the Atlantic to the Pacific Oceans and spanning a range of elevations (Fig. 1*B*) (see *Materials and Methods*) and analyzed them using a Monte Carlo Principal Component (MCPC) approach (27–29). The records include $\delta^{18}O$ of ice (30, 31), speleothems (7, 15, 21, 32–44), and lake sediment (14, 16, 17, 45–53); carbon isotope ($\delta^{13}C$) values of speleothems (7, 15, 21, 32, 34, 36, 38, 43, 44); δD of lake sediment (18, 54); ocean sediment trace metal concentrations (55); lake sediment lithology and/or bio/geochemistry (56–58); multiproxy paleolimnological data (59); diatoms in lake sediment (60); and ice accumulation data (61) (*SI Appendix*, Table S1). Each of the paleoclimate proxies was interpreted by the primary authors to reflect changes in hydroclimate, although they vary in their uncertainties as well as the geographic scale of information provided.

Three distinct proxy ensembles were analyzed: ALL, which consists of all records ($n = 48$); PRECIP$\delta^{18}O$, which consists exclusively of records of changes in the isotopic composition of precipitation archived in ice, speleothems, and lake sediment ($n = 21$); and NON-PRECIP$\delta^{18}O$, which consists of records other than those reflecting precipitation isotope values ($n = 27$). The latter two ensembles were analyzed to determine the influence of proxy type on the results. Within each ensemble, the records were separated into three groups that were each independently analyzed: those currently located directly within the ITCZ core region (hereafter referred to as "Core"), those located in the northern tropics and outside of the ITCZ Core region ("Northern"), and those located in southern tropics and outside of the Core region ("Southern"). These groupings were chosen to test hypotheses related to ITCZ width/strength versus mean position changes.

MCPC analysis of the ALL ensemble returned positive median Empirical Orthogonal Function (EOF)–1 loadings for 11 of 18 Northern records, negative loadings for 19 of 21 Southern records, and positive loadings for 8 of 9 Core records onto PC1 (~47% of variance) (Fig. 2 *A* and *B* and *SI Appendix*, Fig. S1 and Table S2). PC1 of the Northern records (~51% of variance) demonstrates relatively wetter conditions during what is often termed the Medieval Climate Anomaly (MCA; ~950 to 1250 CE) (13), while PC1 of the Southern records (~42% of variance) indicates drier conditions during this time, with the opposite pattern during the LIA. PC1 of the Core records indicates relatively wetter conditions during the MCA and a transition to a drier climate thereafter, largely consistent with the Northern PC1 pattern. The Northern and Southern PC1 series are strongly anti-correlated ($r = -0.93$
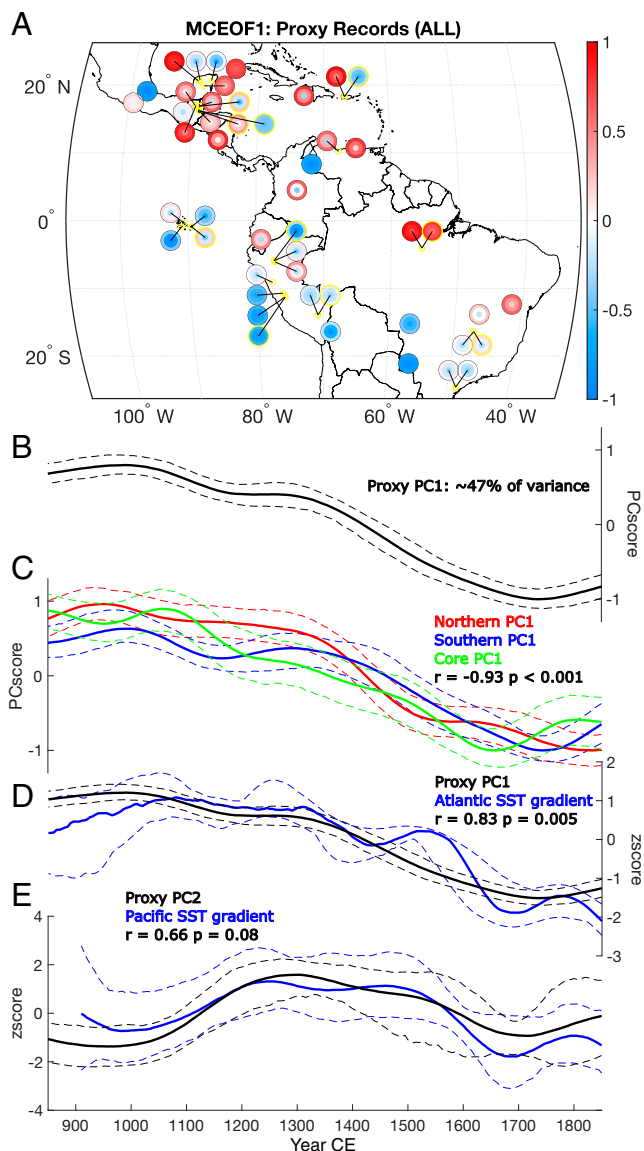
Fig. 2. Results from neotropical paleoclimate record analysis. (*A*) Paleoclimate proxy MCEOF1 loadings (circles) onto MCPC1 of the ALL ensemble. The outer ring, inner ring, and central colors depict the 2σ high, median, and 2σ low loading values, respectively. Circles outlined in yellow are speleothem $\delta^{13}C$, ice accumulation for the Quelccaya Ice Cap, and lipid δD for El Junco Lake. (*B* and *C*) Median (solid) and 2σ range (dashed) of MCPC1 for (*B*) All, (*C*) Northern (red), Southern (blue; multiplied by −1 for visual comparison), and Core (green) records from the ALL proxy ensemble. (*D*) Median (solid black) and 2σ range (dashed black) of proxy MCPC1 and median (solid blue) and 2σ range (dashed blue) of 1,000 realizations of the Atlantic meridional SST gradient (north – south). (*E*) Median (solid black) and 2σ range (dashed black) of MCPC2 and median (solid blue) and 2σ range (dashed blue) of 1,000 realizations of the Pacific zonal SST gradient (west – east).

2σ: −0.85 to −0.98, $P < 0.001$) (Fig. 2*C*; see *Materials and Methods*), suggesting opposite hydroclimate changes in each hemisphere.

Relative to the Southern records, those in the Northern group exhibit substantial heterogeneity in their EOF ranges. Closer inspection, however, reveals that seven of the Northern EOF ranges are entirely positive versus four that are entirely negative, and a parallel analysis of the difference between Northern proxy values from the LIA and MCA shows that the former time period was relatively dry (i.e., the LIA to MCA difference ranges are entirely negative) in 6 of the 18 locations

versus 3 that show wetter conditions (*SI Appendix*, Fig. S2). This suggests that although there is substantial variability among the Northern records, the general pattern is a transition to a drier climate during the LIA. The coherency among the Southern records is likely at least in part a result of the abundance of PRECIPδ^{18}O records [which capture broad, regional-scale processes associated with the SAM (7)] in that group, while the relative heterogeneity among the Northern records is likely due to complex, locally controlled processes related to topography (62), coastal proximity, and associated atmospheric circulation (26), as well as the greater diversity of proxy types and the disparities in specific hydroclimate information they record (see *Materials and Methods*).

Consistent with MCPC1 of the ALL ensemble, MCPC1s for both the PRECIPδ^{18}O and NON-PRECIPδ^{18}O (*SI Appendix*, Figs. S3 and S4) ensembles exhibit a decreasing trend over the last millennium. There are, however, notable differences; for example, the PRECIPδ^{18}O MCPC1 has a prominent maximum at ~1000 CE, while the NON-PRECIPδ^{18}O MCPC1 declines through this interval before reaching a local maximum around 1350 CE, a feature driven by variability in the nine Southern records (note that Southern MCPC1 values were multiplied by −1 for comparison in the figures). This suggests dry conditions prevailed around 1350 CE at the NON-PRECIPδ^{18}O locations having positive loadings onto MCPC1 and that the PRECIPδ^{18}O records from those sites (or nearby) do not reflect local climate. This could have resulted from upstream rainout and isotopic depletion of air masses prior to reaching the locations of the archives. Additionally, the relatively small number of Southern records in the NON-PRECIPδ^{18}O ensemble makes it less useful for reconstructing large-scale hydroclimate patterns. The ALL ensemble, on the other hand, has the advantage of a greater number and spatial distribution of records as well as a larger variety of proxy types.

To test whether paleoclimate evidence supports an ocean temperature control of ITCZ position, changes in the Atlantic meridional SST gradient over the last millennium are inferred from the difference between reconstructions of SST north of Iceland (63) and the eastern Southern Ocean (64) (Note that no other non-coastal South Atlantic records exist that have sufficient temporal resolution.) (Fig. 2*D* and *SI Appendix*, Figs. S3*D* and S4*D*). These data indicate relative warming of the South Atlantic during the transition into the LIA and an SST pattern consistent with a southerly displaced ITCZ. The strong correlation ($r = 0.83$ 2σ: 0.72 to 0.91, $P = 0.005$ for ALL) between the proxy PC1 and the Atlantic meridional SST gradient supports this inference. A reconstruction of the zonal SST gradient in the tropical Pacific (65) indicates relative warming of the east Pacific cold tongue region during the LIA (Fig. 2*E* and *SI Appendix*, Figs. S3*E* and S4*E*), which would promote an El Niño–like mean state and a southward displacement of the ITCZ. Proxy PC2 and the Pacific zonal SST gradient exhibit several notable parallels ($r = 0.66$ 2σ: 0.15 to 0.90, $P = 0.08$ for ALL), including lower values during the LIA, suggesting a secondary but important role for tropical Pacific ocean–atmosphere dynamics in controlling neotropical precipitation on long timescales.

Climate Model Analysis: All-Forcing Experiments. To investigate hypothesized ITCZ responses to the combined effects of prominent external forcings, we compared our paleoclimate record synthesis to results from the Community Earth System Model [CESM1-LME Last Millennium Ensemble (LME) (66)]. By conducting principal component (PC) analysis on the ensemble mean rather than individual simulations, the influence of internal variability on the results is reduced, given that internal (i.e., random) signals largely cancel across an average of many model realizations (in this case 13) using the same external forcings (67–69). The results reveal spatiotemporal precipitation patterns that are generally similar to results from the paleoclimate record analysis. Both EOF1 (Fig. 3*A*) and EOF2 (*SI Appendix*, Fig. S5*A*) of modeled annual precipitation indicate north-south antiphasing on multicentury timescales, although in the case of EOF1, South America as a whole varies in phase, a pattern somewhat inconsistent with the paleoclimate data. Model PC1 indicates a shift from wetter to drier conditions in much of the Northern region, and vice versa in the Southern region, during the transition into the LIA (Fig. 3*B*). Furthermore, precipitation PC1 is strongly correlated to the Atlantic meridional SST gradient (north − south) ($r = 0.83$, $P = 0.003$), which is expressed through EOF2 of model SST and exhibits a north-south antiphasing pattern (Fig. 4*A*), with the corresponding PC2 of SST similar to both model precipitation PC1 and the Atlantic meridional SST gradient (Fig. 3*B*). PC3 of Pacific-Indian tropical SST (Fig. 3*C*) significantly correlates ($r = -0.65$, $P = 0.043$, linear trend removed from both series) with PC2 of model precipitation, and the associated EOF exhibits an interhemispheric, antiphased loading pattern (Fig. 4*E*). These results suggest that changes in Atlantic basin SST are the predominant control on precipitation variability in the tropical Americas on multicentury timescales and that Pacific basin processes are an important but secondary influence, similar to the relationships identified in the paleoclimate records.

Climate Model Analysis: Single-Forcing Experiments. The CESM1-LME single-forcing (volcanic and solar) ensemble means (five and four simulations, respectively) provide an experimental framework for investigating the impact of individual external forcings on ocean-atmosphere circulation and the resulting influence on hydroclimate in the tropical Americas. The volcanic-only precipitation EOF1 pattern displays a distinct north-south antiphased structure similar to that of the all-forcing pattern (Fig. 3*D*), whereas the solar-only EOF1 pattern displays an east-west antiphased signature across much of tropical South America (Fig. 3*G*). Additionally, the correlation between PC1 of precipitation for the volcanic-only and all-forcing simulations is significant ($r = 0.66$, $P = 0.038$), while that between the solar-only and all-forcing ensembles is not ($r = 0.04$, $P = 0.91$) (both correlations over the interval 900 to 1800 CE). Although precipitation PC1 is significantly correlated to the Atlantic meridional SST gradient (north − south) in both the volcanic-only (Fig. 3*E*) and solar-only (Fig. 3*H*) ensembles, the correlation is substantially stronger for the volcanic-only scenario ($r = 0.79$, $P = 0.006$ versus $r = 0.67$, $P = 0.033$). Analysis of both of the single-forcing simulation ensembles reveals significant correlations between Pacific–Indian basin SST and precipitation in the tropical Americas. For each experiment, PC2 of precipitation significantly correlates with either SST PC2 (volcanic-only: $r = -0.58$, $P = 0.077$) (Fig. 3*F*) or PC3 (solar-only: $r = -0.76$, $P = 0.01$) (Fig. 3*I*), although the SST EOF patterns are inconsistent with one another and with that of the all-forcing simulations.

Patterns of ITCZ Variability during the Last Millennium and Controlling Mechanisms. These results strongly suggest that tropical American hydroclimate over the last millennium was driven by a common mechanism capable of producing large-amplitude latitudinal fluctuations that persisted for centuries. Externally forced variability in the location of the ITCZ and its interaction with the monsoon systems provide such a
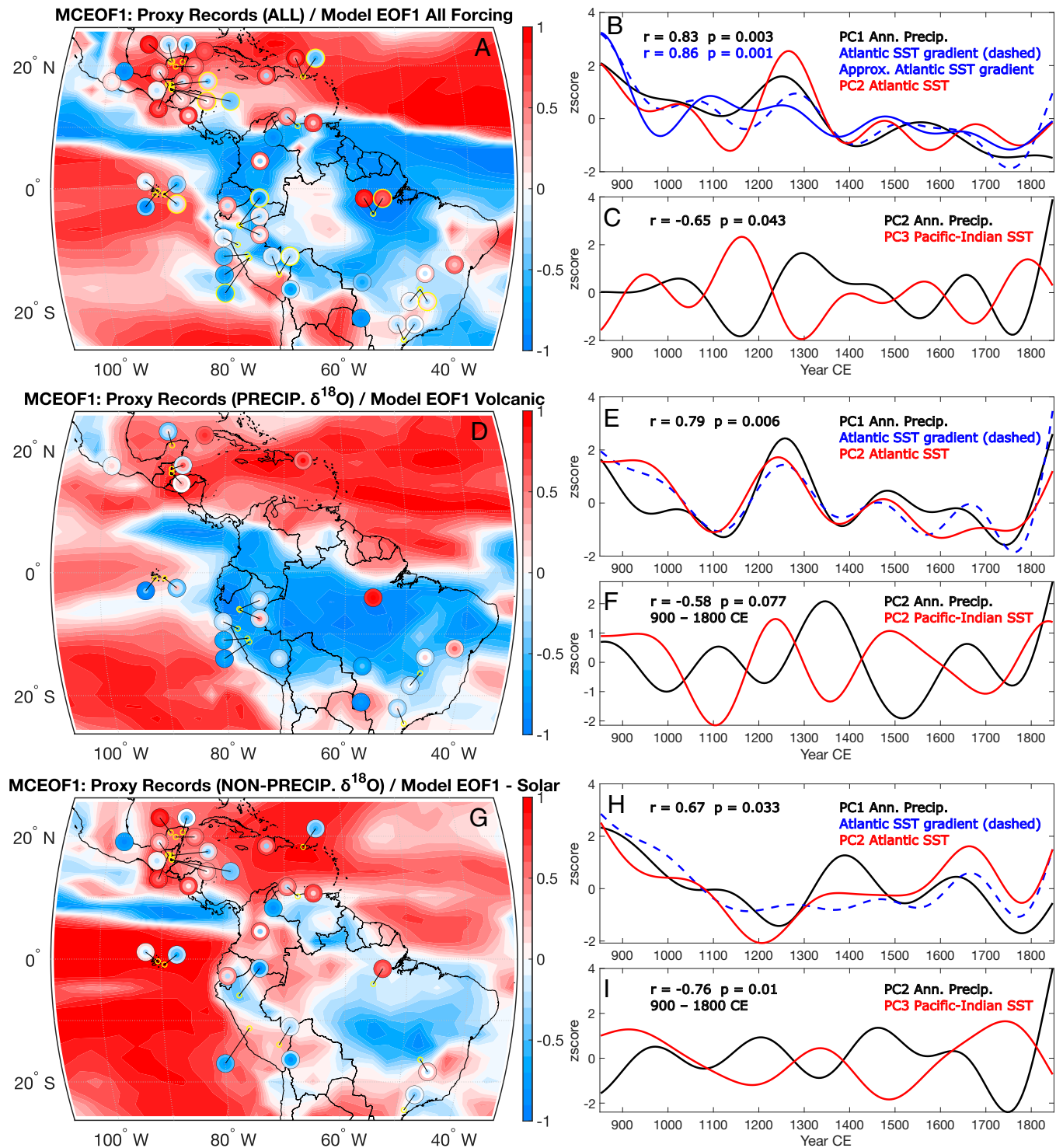
Fig. 3. Results from neotropical paleoclimate data and CESM1-LME analyses. (*A*) Paleoclimate record MCEOF1 loadings onto MCPC1 of the ALL ensemble (circles as described in Fig. 2). Background colors: EOF1 loadings for each grid cell onto PC1 of the annual precipitation field in the CESM1-LME all-forcing simulations. (*B*) Model PC1 of precipitation in the tropical Americas (black), meridional (north – south) Atlantic SST gradient (dashed blue), approximation (Approx.) of the meridional Atlantic SST gradient (solid blue) from a weighted combination of the global, interhemispheric mean temperature difference (north – south) and maximum North Atlantic streamfunction (series shown in *SI Appendix*, Fig. S6*C*), and PC2 of Atlantic basin SST (red). (*C*) Model PC2 of precipitation in the tropical Americas (black) and PC2 or PC3 of Pacific–Indian tropical SST (red) (linear trend removed from both series). For *B*, the correlations are between the regression model and the meridional Atlantic SST gradient (blue text) and PC1 of precipitation and the meridional Atlantic SST gradient (black text). (*D–F*) PRECIP δ¹⁸O proxy and volcanic-only model results. (*G–I*) NON-PRECIP δ¹⁸O proxy and solar-only model results. The 200-y low-pass filter was applied to all series prior to analysis. EOFs corresponding to the Atlantic and Pacific–Indian SST PC and precipitation PC2 for each ensemble are shown in Fig. 4 and *SI Appendix*, Fig. S5, respectively. Ann. Precip., annual precipitation.

mechanism. MCPC analysis of the paleoclimate data indicate that both the Northern and Core regions were relatively dry during the LIA. Theoretical and modeling studies suggest that ITCZ width and strength are linked, with a wider latitudinal distribution coupled with reduced precipitation intensity and vice versa (3). The reduction in Core region precipitation is thus consistent with the hypothesis that the ITCZ became wider and weaker during the LIA (21). However, this would

also, in theory, have led to an increase in precipitation along the equatorward margins of both the Northern and Southern regions (i.e., where locations are most sensitive to ITCZ position and/or width changes). While the Southern records, spanning a broad latitudinal range, generally indicate greater precipitation and a wetter overall climate during the LIA, there is no conclusive evidence of wetter conditions along the equatorward edge of the Northern region. For example, records from the southern Yucatan exhibit no clear trend and, in some cases, contradictory patterns [see Yok Balum G δ^{13}C (21) and Macal Chasm δ^{18}O (34), among others] (*SI Appendix*, Figs. S1 and S2). The paleo-data therefore do not support the hypothesis that ITCZ width changes were the principal control on hydroclimate in the neotropics during the past millennium (and during the LIA in particular). Rather, they point toward a more complex response characterized by a southward shift in the mean position of the ITCZ coupled with a reduction in strength within the Core region and local climate controls in Central America that, in some locations, appears to predominate over the broad, synoptic-scale influences expected from changes in the ITCZ. In the northern neotropics, several controls add complexity to precipitation dynamics and thus may help to explain differences between the records, including

variations in the Atlantic–Pacific cross-basin SST gradient and the resulting shifts in interbasin atmospheric circulation (29), the direct influence of the Atlantic Warm Pool on precipitation in the Yucatan region during the fall (after the ITCZ has migrated to the south) (62), and enhanced local rainout during topographic uplift on Caribbean-facing mountains in response to strengthened trade winds (which commonly occur when the ITCZ is shifted southward) (71).

That proxy MCPC1 most strongly corresponds to the Atlantic (rather than Pacific) SST pattern points toward processes operating in the Atlantic basin as the principal drivers. This result is consistent with patterns identified in the climate model simulations, wherein PC1 of neotropical precipitation strongly corresponds with PC2 of Atlantic basin SST, while PC2 (which explains substantially less total variance; *SI Appendix*, Table S2) of model precipitation exhibits similarity to either PC2 or PC3 of Pacific–Indian basin SST (depending on the external forcing scenario) (Fig. 4). A more compelling proxy-data comparison would involve multiple high-resolution SST datasets from the tropical South Atlantic, from which there are none currently, and additional records from the eastern tropical Pacific region (72), given the limited utility of basin-scale temperature gradients based on a small number (e.g.,) of SST records.
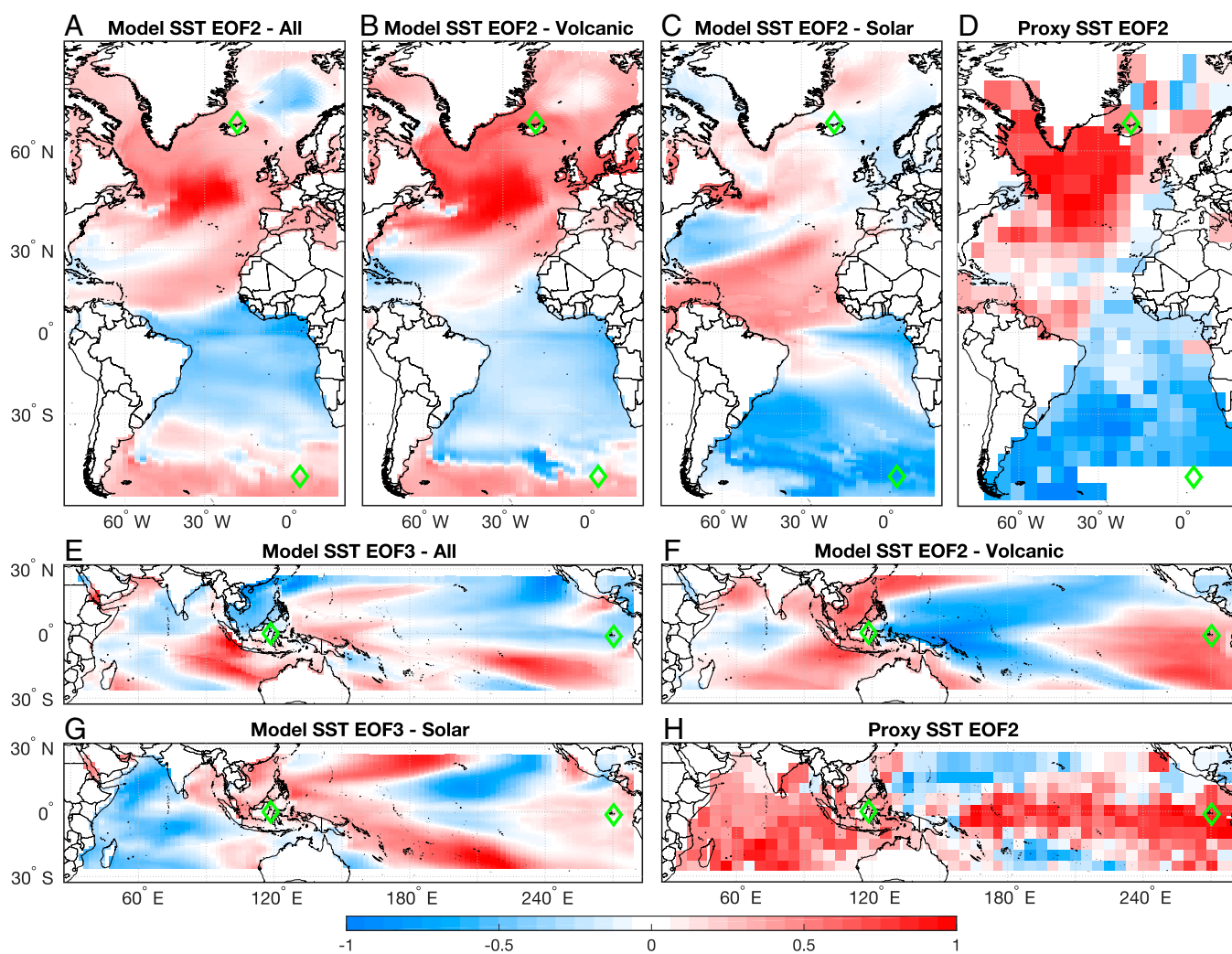
Fig. 4. Results from the CESM1-LME mean and proxy-based climate field reconstruction of Mann et al. (70). (*A–D*) EOF2 of Atlantic Basin SST for (*A*) all-forcing, (*B*) volcanic-only, and (*C*) solar-only simulations and (*D*) proxy data. (*E–H*) Tropical Pacific–Indian SST (*E*) EOF3 for all-forcing, (*F*) EOF2 for volcanic-only, (*G*) EOF3 for solar-only, and (*H*) EOF2 for proxy data. Green diamonds, locations of SST records used to produce ocean-basin SST gradient reconstructions shown in Fig. 2.

Volcanic and solar forcing have been shown to be the dominant external controls on climate change during the preindustrial era (70), with volcanism principally responsible for the transition into the LIA (73). While the radiative forcing by explosive tropical volcanic eruptions is largely symmetric with respect to the equator, the response is not. Owing to its larger extent of land coverage and lesser thermal inertia relative to the Southern Hemisphere, there is a greater cooling response to volcanic eruptions in the Northern Hemisphere. This mechanism alone, combined with more numerous and clustered volcanic events, is expected to yield a southward displacement of the thermal equator and the potential for synchronous but antiphased precipitation changes across the tropics during the LIA. Additional dynamical mechanisms appear to play an important role, however, in the model simulations. For example, in the all-forcing experiments, a southward displacement of the thermal equator and an interhemispheric, antiphased pattern of SST variability also are favored by a slowdown in the Atlantic Meridional Overturning Circulation (AMOC) and expansion of sea ice (*SI Appendix,* Fig. S6). A weighted average (produced via multivariate regression) of the global, interhemispheric temperature difference (north − south) and the North Atlantic maximum streamfunction series (i.e., AMOC) approximates the Atlantic SST gradient ($r = 0.86$, $P = 0.001$) and is similar to PC1 of precipitation ($r = 0.73$, $P = 0.016$) (Fig. 3B), indicating that both the direct temperature response to volcanism and the longer timescale ocean response are key controls (70, 73–75). Supporting these results, North Atlantic freshwater forcing experiments conducted by Zhang and Delworth (76) produced a substantial reduction in the AMOC, a relative cooling of the North Atlantic, and an interhemispheric, antiphased precipitation pattern in the tropical Americas consistent with behavior exhibited by the CESM1-LME during the LIA.

The strong similarity between Atlantic SST EOF2 of the volcanic-only (Fig. 4B) and all-forcing ensembles and the relative dissimilarity between the latter and the solar-only SST EOF2 (Fig. 4C) indicates volcanic forcing is the dominant causal mechanism of the antiphased Atlantic SST pattern and thus the principal driver of precipitation and SST variability on centennial timescales. Supporting this assertion, analysis of the Mann et al. (70) proxy-based SST field reconstruction demonstrates an EOF2 pattern (Fig. 4D) that is markedly similar to both the volcanic-only and all-forcing results, but differs from the solar-only results. It is worth noting that the proxy-based reconstruction is based on a small number of spatial EOFs, particularly during the earlier centuries, limiting its ability to capture fine-scale structure in the SST pattern.

EOFs from the volcanic-only experiments display a distinct horseshoe-like pattern that extends across the Pacific basin and resembles the canonical El Niño SST anomaly pattern (Fig. 4F), while the solar-only simulations have a more complex structure with responses in the Indian basin and the central Pacific that are opposite those of the eastern and western sides of the Pacific basin (Fig. 4G), similar to central Pacific (i.e., Modoki) El Niño SST anomalies. Both of these SST arrangements impact zonal wind strength in the Pacific basin, with the former strengthening easterly winds and amplifying the Walker Circulation during eastern Pacific cool phases (and vice versa) and the latter potentially leading to a two-cell Walker circulation and a strengthened convection region in the central Pacific. Analysis of observational data demonstrates highly disparate atmospheric circulation and precipitation responses over South America during the two different expressions of El Niño–Southern Oscillation (ENSO) (77), which potentially explains the disparity between volcanic-only

and solar-only precipitation EOF1, particularly over the northern Andes of Colombia, western Brazil, and the Andes region of southern Peru and Bolivia. The Pacific basin EOF2 pattern in the Mann et al. (70) field reconstruction largely resembles that of the volcanic-only simulations and thus also points toward volcanic forcing as the dominant external control on Pacific ocean–atmosphere variability on multicentury and longer timescales.

Conclusions

Paleoclimate data indicate that a multicentury-long southerly shift in the ITCZ accompanied by a decrease in ITCZ strength occurred in the neotropics over the past millennium in response to relative cooling of the Northern Hemisphere, culminating in the early 18th century (Fig. 2 *C* and *D*). This finding is in contrast to recent studies that use changes in ITCZ width and/or strength to explain inferred tropical precipitation patterns in both the neotropics (21) and Asia (22–24) and reinforces recent conclusions based on model (25) and proxy data (78) that ITCZ responses to external forcing are region specific. Exhibiting a similar north-south antiphasing pattern of precipitation, the single and all-forcing simulations from CESM1-LME reveal that volcanic forcing was the principal driver of hydroclimate and ITCZ changes over the last millennium and that Atlantic basin processes, in particular changes in the meridional SST gradient, were the main ocean–atmosphere controls. The development of additional well-dated paleoclimate records of catchment-scale precipitation-evaporation balance from the Andes and Amazon basin, along with additional records of all types, and in particular precipitation $\delta^{18}O$ values, from the northern neotropics should help to better characterize ITCZ behavior over past centuries and shed light on potential future responses of the tropical rain belt to anthropogenic radiative forcing.

Materials and Methods

Modern Precipitation Trends. Three land station–based observational data products were used to produce the precipitation time series: University of Delaware Terrestrial Precipitation: 1900-2017 Gridded Monthly Time Series V5.0.1 (79); Global Precipitation Climatology Centre (GPCC) Full Data Reanalysis Version 2018 (80); and Climatic Research Unit TS4.02 Precipitation (81). All three datasets have $0.5 \times 0.5°$ spatial resolution and span a common time period of 1901 through 2016 CE. The mean across the three products was computed for each grid cell, and trends were determined for each grid cell via linear regression (see Correlation and Significance Methods below) for annual (Fig. 1A) October to March (*SI Appendix,* Fig. S7A) and April to September (*SI Appendix,* Fig. S7B) total precipitation.

Record Selection. The criteria for inclusion in the MCPC analysis were a minimum temporal resolution of 50 y, a minimum of two age model control points (excluding extraction age), a time frame that encompasses 850 to 1850 CE (with three exceptions; see Hydroclimate Record Realizations below), and a location within 25S to 22.5N and 40W to 100W. The ALL ensemble includes all the records. The PRECIP$\delta^{18}O$ ensemble consists of records that reflect changes in the isotopic composition of precipitation [including the δD records of Sachs et al. (18) and Nelson and Sachs (54)]. For these records, we assumed isotopic equilibrium between meteoric water source and the analyzed material (45, 82), even in the case of the Macal Chasm $\delta^{18}O$ record (34), which is known to have been influenced by kinetic fractionation but nevertheless contains a strong precipitation $\delta^{18}O$ signal. The NON-PRECIP$\delta^{18}O$ ensemble consists of records that do not mainly reflect precipitation isotope values and therefore represent changes in catchment-scale hydroclimate.

Paleoclimate Proxy Influences and Uncertainties. Most of the records (29 of 48) are from ice core, lake sediment, or speleothem $\delta^{18}O$ measurements. $\delta^{18}O$ from speleothems and open-basin lakes and δD from terrestrial organic material in lake sediments predominantly reflect the isotopic composition of

precipitation, which is controlled (via Rayleigh distillation) by the extent of rainout (i.e., precipitation amounts) along the moisture transport pathway and the amount of precipitation (via the "amount effect") at the archive location (7). Andean ice core, speleothem, and lake sediment $\delta^{18}O$ measurements are therefore interpreted as predominantly recording the $\delta^{18}O$ of air masses traversing tropical South America, with a strong influence by the isotopic effects of monsoonal precipitation and moisture recycling in the Amazon basin (7). Sources of uncertainty include potential isotopic disequilibrium between precipitation/groundwater and either the carbonate minerals (82) or organic material (18) preserved in speleothem or sediment, respectively, as well as secondary influences on air mass isotope content by temperature and evaporation. $\delta^{18}O$ records from closed-basin lakes are most strongly influenced by changes in lake hydrologic balance and the extent to which water losses occur through evaporation (49). Isotopic disequilibrium between water and calcite forming in the water column, as well as changes in the isotopic composition of inflowing meteoric water, are potential sources of uncertainty in closed-basin lake $\delta^{18}O$ records (83). The sediment lithology (56), ice accumulation (61), and speleothem $\delta^{13}C$ (51) records reflect hydroclimate on a local/catchment scale and thus should be expected to exhibit patterns that are at least somewhat different from those of the precipitation $\delta^{18}O$ records. The proxy controls described above hold true at interannual to orbital timescales and are supported by modeling results (7, 82).

Hydroclimate Record Realizations. Paleoclimatic data have several limitations related to both the sensitivity of the proxy to specific climate variables (as discussed above) and, perhaps most importantly, the inherent age model uncertainty, which is derived from the analytical uncertainty of radiometric ages and the uncertainty associated with age assignments for proxy values between dated layers (due to, for example, unknown changes in the rate of archive accumulation). To better resolve these issues, in our MCPC analysis we leveraged the power of age-modeling routines that characterize uncertainty both in age control points and archive deposition rates to produce a large ensemble of realizations for each paleoclimate record.

For each record, 1,000 age model realizations were produced using Bchron (84) (version 4.7.6, compiled in R), which accounts for both analytical and calibration-related uncertainty in age control point data as well as potential changes in accumulation rates of the archives. Bchron has been shown to produce age models similar to those of other software packages based on Bayesian methods (85). Insufficient data were available for one of the speleothem records (Dos Anas); consequently, age model uncertainty was not applied to this record. The Quelccaya and Huascarán ice core datasets were dated using layer counting and/or flow modeling. To account for uncertainty in these records, an algorithm was applied that assumes a 1% likelihood of either missing a layer/year entirely or falsely identifying a layer/year. For speleothem records produced by combining data from independent speleothems (either from the same cave or different cave systems), 1,000 realizations of each of the separate records were produced, and the data were spliced at a year near the midpoint of the overlapping time frame. Time gaps in spliced speleothem records, which occasionally occurred due to age model uncertainty, were infilled using linear interpolation between the values on each side of the gap. For records that did not span the entire 850 to 1850 CE interval (i.e., Cascayunga, Perdida, Cariaco), end values (i.e., nearest neighbor) were used to infill the missing time periods. Unless otherwise noted, the age model data correspond to that of the original sources and were obtained either from public databases [National Oceanic and Atmospheric Administration, National Centers for Environmental Information (NOAA-NCEI) and the Speleothem Isotopes Synthesis and AnaLysis (SISAL) working group (86)] or through communication with the researchers. Intcal20 (87) was used for ^{14}C age calibration. Unless otherwise noted, all computations were performed in MATLAB.

The 1,000 age model realizations for each hydroclimate record were used to produce 1,000 realizations of each record (i.e., one proxy times series was produced for each of the 1,000 age models). One thousand different ensembles of the 48 records were then compiled using the 1,000 different realizations of each record, with the resulting master ensemble having $n = 48$ members and $r = 1,000$ realizations of each member. Analytical uncertainty values of 0.1 ‰, 0.06 ‰, and 1% (1σ) were applied to the $\delta^{18}O$, $\delta^{13}C$ data, and sediment composition measurements, respectively. Analytical uncertainty was not applied to the other proxies. Each realization was linearly interpolated to a 5-y spacing. To alleviate between-site differences in the amplitude of hydroclimate

reconstructions, each proxy realization was converted to standardized deviation units, or z-scores, where $z = (x - m)/\sigma$ and x, m, and σ are the original data, mean values for individual time series (spanning 850 to 1850 CE), and their SDs, respectively. A 200-y periodicity low-pass filter (88) was applied to each realization in order to isolate multicentury and longer timescale variability.

For the time period difference analysis (i.e., LIA minus MCA), for each realization of each record the mean of the MCA (950 to 1250 CE) was subtracted from the mean of the LIA (1450 to 1850 CE). The median and 2σ range of the resulting distribution was then determined (*SI Appendix*, Fig. S2).

MCPC Analysis. MCPC (27, 28) was conducted on each of the 1,000 sets of realizations of the paleoclimate records to produce synthetic spatial, EOF (also described as "loadings"), and temporal PC variables that capture cumulative (but independent) proportions of variance. For each set, singular value decomposition was applied to compute PCs, EOFs, and eigenvalues (which were subsequently normalized). Empirical distributions of the PCs, EOFs, and normalized eigenvalues at each time step were computed to determine median values and the 1/2σ uncertainty ranges. MCPC was conducted on each set of records and then on records from the Northern, Southern, and Core groups independently. Note that Tierney et al. (27) and Anchukaitis and Tierney (28) describe their method as "Monte Carlo Empirical Orthogonal Function (MCEOF)" rather than MCPC, but the methods are essentially the same. We focused on two climate intervals, the LIA and MCA, that are acknowledged as important in the Northern Hemisphere as a convenience for framing our analysis of the MCPC results for the last millennium.

SST Gradient Reconstructions. The Atlantic meridional SST gradient record was produced using the Southern Ocean SST reconstruction of Nielsen et al. (64) based on analysis of diatoms in Ocean Drilling Program (ODP) sediment core TN057-17 and the North Atlantic SST reconstruction of Sicre et al. (63) based on analysis of alkenones in sediment core MD99-2275. One thousand age model realizations of the Southern Ocean SST reconstruction were produced using Bchron to account for age model uncertainty. Chronological control for the North Atlantic SST record is based on a series of tephra layers dated using dendrochronology; thus, no age uncertainty was applied to this record. One thousand realizations of the Atlantic meridional SST gradient were produced by subtracting each of the 1,000 realizations of the South Atlantic time series from the North Atlantic time series (north – south). We produced 1,000 realizations of the Pacific zonal SST reconstruction (west – east) by randomly sampling from the 2σ uncertainty ranges of the temperature values of Rustic et al. (65). One thousand realizations of both the zonal Pacific and meridional Atlantic SST gradients were used in the correlation and significance assessments.

Correlation and Significance Methods. The Pearson correlation coefficient was used to determine the linear correlation between variables. To determine the effective degrees of freedom (DOF$_{eff}$) for low-pass filtered time series, the inverse of the low-pass filter period was assumed to be the Nyquist frequency, which is defined as half of the sampling rate. DOF$_{eff}$ is therefore defined as

$$DOF_{eff} = 2 * L/LPP - 2$$

where L is the length of the time series and LPP is the low-pass filter period.

For the observational data, no low-pass filtering was applied, and the DOF was adjusted based on the decorrelation time (DT), which is defined as

$$DT = (1 + \rho)/(1 - \rho)$$

where ρ is the lag-1 autocorrelation. The DOF$_{eff}$ is thus defined as

$$DOF_{eff} = DOF/DT - 2$$

DOF$_{eff}$ was applied to determine significance of correlation coefficient values.

For the proxy data, correlation (r) and significance (P) values were calculated for each of the 1,000 sets of correlations between different realizations. The reported values in the text and figures are the mean of the resulting 1,000 r and P values.

Climate Model Analyses. The CESM version 1.1 using the Community Atmosphere Model version 5 was applied in the CESM1-LME (66). The model uses an ~2° resolution for the atmosphere and land components and an ~1° resolution for the ocean and sea ice. The model was spun up for 650 y using boundary conditions for 1850 CE followed by a 200-y spin-up using boundary conditions for

850 CE. The transient LME simulations were branched off from the end of this spin-up. The applied forcings in the all-forcing simulations included orbital, solar, volcanic, changes in land use/land cover, and greenhouse gases. We chose CESM1-LME for this study because it has the advantage of being to date the largest ensemble of last millennium simulations and includes separate ensembles of single-forcing experiments (each with four or five simulations) of sufficient size for internal variability signals to be substantially reduced when averaging across the ensembles, as discussed below.

The separation of internally generated (e.g., ENSO) and externally forced climate signals has been shown (67, 68) to be difficult in principal and an obstacle to the assessment of climate responses to external forcing. We therefore used the mean of the all-forcing and single-forcing simulations for analysis of climate variables (precipitation, SST, North Atlantic streamfunction, and sea ice coverage). The advantage of using the ensemble mean is that even in the case of small ensembles (e.g., four or five members), internal variability signals largely cancel when averaged across multiple simulations (especially when smoothing is applied) (69), and the external forcing signal is thus better isolated.

Monthly average data were used to produce annual averages. To prevent splitting of the hydrologic year in South America, annual averages of precipitation and SST were based on April through March (of the following year). The annual average series from each grid cell in each realization of the ensemble were averaged to produce the ensemble mean. The annual mean time series for each model grid cell were low-pass filtered (88) at a 200-y periodicity prior to PC analysis.

The model Atlantic meridional SST gradient was calculated by subtracting the mean of SST time series in the South Atlantic (0 to 60° S, 310 to 15° E) from the mean of SST in the North Atlantic (0 to 70° N, 305 to 350° E).

The cosine of latitude was applied as a weighting factor for calculations of model mean time series across a spatial domain, and the square root of cosine latitude was applied in the PC analyses of model time series.

The % variance explained for the SST PC-EOFs was determined with PC1 both included and excluded to assess proportions of variance explained among PCs that do not capture the global cooling trend (*SI Appendix*, Table S2).

Filtering Frequency. To assess the influence of the filtering frequency on the results, we produced a complementary set of proxy and precipitation field MCPC results using a 100-y low-pass filter (*SI Appendix*, Fig. S8). The results demonstrate that the conclusions were not dependent upon a specific filter frequency.

Data Availability. All raw data and results from this study, as well as all Matlab code, are available at Penn State Data Commons (https://www.datacommons.psu.edu/commonswizard/MetadataDisplay.aspx?Dataset=6340).

Author affiliations: [a]Department of Earth and Environmental Sciences, University of Minnesota Duluth, Duluth, MN 55812; [b]Large Lakes Observatory, University of Minnesota Duluth, Duluth, MN 55812; [c]Department of Earth, Atmosphere and Environment, Northern Illinois University, DeKalb, IL 60115; [d]Department of Meteorology and Atmospheric Science, The Pennsylvania State University, State College, PA 16802; [e]Department of Earth and Atmospheric Sciences, University of Alberta, Edmonton, AB T6G 2E3, Canada; [f]Department of Geology and Environmental Science, University of Pittsburgh, Pittsburgh, PA 15260; [g]Department of Atmospheric and Environmental Sciences, University at Albany State University of New York, Albany, NY 12222; [h]Department of Earth Sciences, Indiana University–Purdue University, Indianapolis, IN 46202; and [i]Department of Geoscience, University of Nevada, Las Vegas, NV 89154

1. World Food Programme, *Food Security and Emigration: Why People Flee and the Impact on Family Members Left Behind in El Salvador, Guatemala and Honduras* (World Food Programme, Rome, Italy, 2017). https://www.ncbi.nlm.nih.gov/pmc/articles/PMC6279460/. Accessed 15 January 2020.
2. A. Sena *et al.*, Drought in the semiarid region of Brazil: Exposure, vulnerabilities and health impacts from the perspectives of local actors. *PLoS Curr.* **10**, ecurrents.dis.c226851ebd64290e619a4d1ed79c8639. (2018).
3. M. P. Byrne, A. G. Pendergrass, A. D. Rapp, K. R. Wodzicki, Response of the intertropical convergence zone to climate change: Location, width, and strength. *Curr. Clim. Change Rep.* **4**, 355–370 (2018).
4. E. Kalnay *et al.*, The NCEP/NCAR 40-year reanalysis project. *Bull. Am. Meteorol. Soc.* **77**, 437–471 (1996).
5. A. Gruber, Fluctuations in the position of the ITCZ in the Atlantic and Pacific Oceans. *J. Atmos. Sci.* **29**, 193–197 (1972).
6. R. Geen, S. Bordoni, D. S. Battisti, K. Hui, Monsoons, ITCZs, and the concept of the global monsoon. *Rev. Geophys.* **58**, e2020RG000700 (2020).
7. M. Vuille *et al.*, A review of the South American monsoon history as recorded in stable isotopic proxies over the past two millennia. *Clim. Past* **8**, 1309–1321 (2012).
8. T. Schneider, T. Bischoff, G. H. Haug, Migrations and dynamics of the intertropical convergence zone. *Nature* **513**, 45–53 (2014).
9. S. M. Kang *et al.*, The response of the ITCZ to extratropical thermal forcing: Idealized slab-ocean experiments with a GCM. *J. Clim.* **21**, 3521–3532 (2008).
10. A. J. Broccoli, K. A. Dahl, R. J. Stouffer, Response of the ITCZ to Northern Hemisphere cooling. *Geophys. Res. Lett.* **33**, L01702 (2006).
11. R. Shekhar, W. R. Boos, Improving energy-based estimates of monsoon location in the presence of proximal deserts. *J. Clim.* **29**, 4741–4761 (2016).
12. A. E. Putnam, W. S. Broecker, Human-induced changes in the distribution of rainfall. *Sci. Adv.* **3**, e1600871 (2017).
13. V. Masson-Delmotte *et al.*, "Information from paleoclimate archives" in *Climate Change 2013: The Physical Science Basis. Contribution of Working Group I to the Fifth Assessment Report of the Intergovernmental Panel on Climate Change*, T. F. Stocker et al., Eds. (Cambridge University Press, 2014), pp. 383–464.
14. D. A. Hodell *et al.*, Reconstruction of Caribbean climate change over the past 10,500 years. *Nature* **352**, 790–793 (1991).
15. A. Winter *et al.*, Evidence for 800 years of North Atlantic multi-decadal variability from a Puerto Rican speleothem. *Earth Planet. Sci. Lett.* **308**, 23–28 (2011).
16. D. A. Hodell *et al.*, Climate change on the Yucatan Peninsula during the Little Ice Age. *Quat. Res.* **63**, 109–121 (2005).
17. N. D. Stansell, B. A. Steinman, M. B. Abbott, M. Rubinov, M. Roman-Lacayo, Lacustrine stable isotope record of precipitation changes in Nicaragua during the Little Ice Age and Medieval Climate Anomaly. *Geology* **41**, 151–154 (2013).
18. J. P. Sachs *et al.*, Southward movement of the Pacific intertropical convergence zone AD 1400–1850. *Nat. Geosci.* **2**, 519–525 (2009).
19. F. A. Lechleitner *et al.*, Tropical rainfall over the last two millennia: Evidence for a low-latitude hydrologic seesaw. *Sci. Rep.* **7**, 45809 (2017).
20. J. L. P. S. Campos *et al.*, Coherent South American monsoon variability during the last millennium revealed through high-resolution proxy records. *Geophys. Res. Lett.* **46**, 8261–8270 (2019).
21. Y. Asmerom *et al.*, Intertropical convergence zone variability in the Neotropics during the Common Era. *Sci. Adv.* **6**, eaax3644 (2020).
22. H. Yan *et al.*, Dynamics of the intertropical convergence zone over the western Pacific during the Little Ice Age. *Nat. Geosci.* **8**, 315–320 (2015).
23. M. L. Griffiths *et al.*, Western Pacific hydroclimate linked to global climate variability over the past two millennia. *Nat. Commun.* **7**, 11719 (2016).
24. N. Scroxton *et al.*, Hemispherically in-phase precipitation variability over the last 1700 years in a Madagascar speleothem record. *Quat. Sci. Rev.* **164**, 25–36 (2017).
25. A. Mamalakis *et al.*, Zonally contrasting shifts of the tropical rainbelt in response to climate change. *Nat. Clim. Chang.* **11**, 143–151 (2021).
26. J. S. Singarayer, S. L. Burrough, Interhemispheric dynamics of the African rainbelt during the late Quaternary. *Quat. Sci. Rev.* **124**, 48–67 (2015).
27. J. E. Tierney, J. E. Smerdon, K. J. Anchukaitis, R. Seager, Multidecadal variability in East African hydroclimate controlled by the Indian Ocean. *Nature* **493**, 389–392 (2013).
28. K. J. Anchukaitis, J. E. Tierney, Identifying coherent spatiotemporal modes in time-uncertain proxy paleoclimate records. *Clim. Dyn.* **41**, 1291–1306 (2013).
29. T. Bhattacharya, S. Coats, Atlantic–Pacific gradients drive last millennium hydroclimate variability in Mesoamerica. *Geophys. Res. Lett.* **47**, e2020GL088061 (2020).
30. L. G. Thompson *et al.*, Late glacial stage and holocene tropical ice core records from Huascaran, Peru. *Science* **269**, 46–50 (1995).
31. L. G. Thompson, E. Mosley-Thompson, W. Dansgaard, P. M. Grootes, The Little Ice Age as recorded in the stratigraphy of the tropical Quelccaya Ice Cap. *Science* **234**, 361–364 (1986).
32. L. C. Kanner, S. J. Burns, H. Cheng, R. L. Edwards, M. Vuille, High-resolution variability of the South American summer monsoon over the last seven millennia: Insights from a speleothem record from the central Peruvian Andes. *Quat. Sci. Rev.* **75**, 1–10 (2013).
33. V. F. Novello *et al.*, Multidecadal climate variability in Brazil's Nordeste during the last 3000 years based on speleothem isotope records. *Geophys. Res. Lett.* **39**, L23706 (2012).
34. P. D. Akers *et al.*, An extended and higher-resolution record of climate and land use from stalagmite MC01 from Macal Chasm, Belize, revealing connections between major dry events, overall climate variability, and Maya sociopolitical changes. *Palaeogeogr. Palaeoclimatol. Palaeoecol.* **459**, 268–288 (2016).
35. V. F. Novello *et al.*, Centennial-scale solar forcing of the South American Monsoon System recorded in stalagmites. *Sci. Rep.* **6**, 24762 (2016).
36. B. E. Wortham *et al.*, Assessing response of local moisture conditions in central Brazil to variability in regional monsoon intensity using speleothem 87Sr/86Sr values. *Earth Planet. Sci. Lett.* **463**, 310–322 (2017).
37. M. Medina-Elizalde *et al.*, High resolution stalagmite climate record from the Yucatán Peninsula spanning the Maya terminal classic period. *Earth Planet. Sci. Lett.* **298**, 255–262 (2010).
38. D. J. Kennett *et al.*, Development and disintegration of Maya political systems in response to climate change. *Science* **338**, 788–791 (2012).
39. C. Fensterer *et al.*, Millennial-scale climate variability during the last 12.5 ka recorded in a Caribbean speleothem. *Earth Planet. Sci. Lett.* **361**, 143–151 (2013).

40. M. S. Lachniet, J. P. Bernal, Y. Asmerom, V. Polyak, D. Piperno, A 2400 yr Mesoamerican rainfall reconstruction links climate and cultural change. *Geology* **40**, 259–262 (2012).

41. J. Reuter *et al.*, A new perspective on the hydroclimate variability in northern South America during the Little Ice Age. *Geophys. Res. Lett.* **36**, L21706 (2009).

42. V. F. Novello *et al.*, Two millennia of South Atlantic Convergence Zone variability reconstructed from isotopic proxies. *Geophys. Res. Lett.* **45**, 5045–5051 (2018).

43. X. Wang *et al.*, Hydroclimate changes across the Amazon lowlands over the past 45,000 years. *Nature* **541**, 204–207 (2017).

44. J. Apaéstegui *et al.*, Hydroclimate variability of the northwestern Amazon Basin near the Andean foothills of Peru related to the South American Monsoon System during the last 1600 years. *Clim. Past* **10**, 1967–1981 (2014).

45. B. W. Bird *et al.*, A 2,300-year-long annually resolved record of the South American summer monsoon from the Peruvian Andes. *Proc. Natl. Acad. Sci. U.S.A.* **108**, 8583–8588 (2011).

46. N. D. Stansell *et al.*, A lake sediment stable isotope record of late-middle to late Holocene hydroclimate variability in the western Guatemala highlands. *Earth Planet. Sci. Lett.* **542**, 116327 (2020).

47. M. F. Rosenmeier, D. A. Hodell, M. Brenner, J. H. Curtis, T. P. Guilderson, A 4000-year lacustrine record of environmental change in the Southern Maya Lowlands, Petén, Guatemala. *Quat. Res.* **57**, 183–190 (2002).

48. M. W. Binford *et al.*, Climate variation and the rise and fall of an Andean civilization. *Quat. Res.* **47**, 235–248 (1997).

49. D. A. Hodell, M. Brenner, J. H. Curtis, Terminal Classic drought in the northern Maya lowlands inferred from multiple sediment cores in Lake Chichancanab (Mexico). *Quat. Sci. Rev.* **24**, 1413–1427 (2005).

50. J. H. Curtis *et al.*, A multi-proxy study of Holocene environmental change in the Maya Lowlands of Peten, Guatemala. *J. Paleolimnol.* **19**, 139–159 (1998).

51. J. H. Curtis, D. A. Hodell, M. Brenner, Climate variability on the Yucatan Peninsula (Mexico) during the past 3500 years, and implications for Maya cultural evolution. *Quat. Res.* **46**, 37–47 (1996).

52. T. Bhattacharya *et al.*, Cultural implications of late Holocene climate change in the Cuenca Oriental, Mexico. *Proc. Natl. Acad. Sci. U.S.A.* **112**, 1693–1698 (2015).

53. J. H. Curtis, M. Brenner, D. A. Hodell, Climate change in the Lake Valencia Basin, Venezuela, ~12600 yr BP to present. *Holocene* **9**, 609–619 (1999).

54. D. B. Nelson, J. P. Sachs, Galápagos hydroclimate of the Common Era from paired microalgal and mangrove biomarker 2H/1H values. *Proc. Natl. Acad. Sci. U.S.A.* **113**, 3476–3481 (2016).

55. G. H. Haug, K. A. Hughen, D. M. Sigman, L. C. Peterson, U. Röhl, Southward migration of the intertropical convergence zone through the Holocene. *Science* **293**, 1304–1308 (2001).

56. C. M. Moy, G. O. Seltzer, D. T. Rodbell, D. M. Anderson, Variability of El Niño/Southern Oscillation activity at millennial timescales during the Holocene epoch. *Nature* **420**, 162–165 (2002).

57. B. W. Bird *et al.*, Paleoclimate support for a persistent dry island effect in the Colombian Andes during the last 4700 years. *Holocene* **28**, 217–228 (2018).

58. D. M. Thompson *et al.*, Tropical Pacific climate variability over the last 6000 years as recorded in Bainbridge Crater Lake, Galápagos. *Paleoceanography* **32**, 903–922 (2017).

59. P. J. Polissar, M. B. Abbott, A. P. Wolfe, M. Vuille, M. Bezada, Synchronous interhemispheric Holocene climate trends in the tropical Andes. *Proc. Natl. Acad. Sci. U.S.A.* **110**, 14551–14556 (2013).

60. J. L. Conroy *et al.*, Unprecedented recent warming of surface temperatures in the eastern tropical Pacific Ocean. *Nat. Geosci.* **2**, 46–50 (2009).

61. L. G. Thompson, E. Mosley-Thompson, J. F. Bolzan, B. R. Koci, A 1500-year record of tropical precipitation in ice cores from the Quelccaya Ice Cap, Peru. *Science* **229**, 971–973 (1985).

62. E. Duarte, J. Obrist-Farner, A. Correa-Metrio, B. A. Steinman, A progressively wetter early through middle Holocene climate in the eastern lowlands of Guatemala. *Earth Planet. Sci. Lett.* **561**, 116807 (2021).

63. M.-A. Sicre, *et al.*, Sea surface temperature variability in the subpolar Atlantic over the last two millennia. *Paleoceanography* **26**, 2011PA002169 (2011).

64. S. H. H. Nielsen, N. Koç, X. Crosta, Holocene climate in the Atlantic sector of the Southern Ocean: Controlled by insolation or oceanic circulation? *Geology* **32**, 317–320 (2004).

65. G. T. Rustic, A. Koutavas, T. M. Marchitto, B. K. Linsley, Dynamical excitation of the tropical Pacific Ocean and ENSO variability by Little Ice Age cooling. *Science* **350**, 1537–1541 (2015).

66. B. L. Otto-Bliesner *et al.*, Climate variability and change since 850 CE: An ensemble approach with the Community Earth System Model. *Bull. Am. Meteorol. Soc.* **97**, 735–754 (2016).

67. B. A. Steinman, M. E. Mann, S. K. Miller, Climate change. Atlantic and Pacific multidecadal oscillations and Northern Hemisphere temperatures. *Science* **347**, 988–991 (2015).

68. M. E. Mann, B. A. Steinman, S. K. Miller, On forced temperature changes, internal variability, and the AMO. *Geophys. Res. Lett.* **41**, 3211–3219 (2014).

69. L. M. Frankcombe, M. H. England, J. B. Kajtar, M. E. Mann, B. A. Steinman, On the choice of ensemble mean for estimating the forced signal in the presence of internal variability. *J. Clim.* **31**, 5681–5693 (2018).

70. M. E. Mann *et al.*, Global signatures and dynamical origins of the Little Ice Age and Medieval Climate Anomaly. *Science* **326**, 1256–1260 (2009).

71. P. R. Waylen, M. E. Quesada, C. N. Caviedes, Temporal and spatial variability of annual precipitation in Costa Rica and the Southern Oscillation. *Int. J. Climatol.* **16**, 173–193 (1996).

72. H. V. McGregor *et al.*, Robust global ocean cooling trend for the pre-industrial Common Era. *Nat. Geosci.* **8**, 671–677 (2015).

73. G. H. Miller *et al.*, Abrupt onset of the Little Ice Age triggered by volcanism and sustained by sea-ice/ocean feedbacks. *Geophys. Res. Lett.* **39**, L02708 (2012).

74. Y. Zhong *et al.*, Centennial-scale climate change from decadally-paced explosive volcanism: A coupled sea ice-ocean mechanism. *Clim. Dyn.* **37**, 2373–2387 (2011).

75. C. F. Schleussner, G. Feulner, A volcanically triggered regime shift in the subpolar North Atlantic Ocean as a possible origin of the Little Ice Age. *Clim. Past* **9**, 1321–1330 (2013).

76. R. Zhang, T. L. Delworth, Simulated tropical response to a substantial weakening of the Atlantic thermohaline circulation. *J. Clim.* **18**, 1853–1860 (2005).

77. R. G. Tedeschi, I. F. A. Cavalcanti, A. M. Grimm, Influences of two types of ENSO on South American precipitation. *Int. J. Climatol.* **33**, 1382–1400 (2013).

78. A. R. Atwood, D. S. Battisti, E. Wu, D. M. W. Frierson, J. P. Sachs, Data-model comparisons of tropical hydroclimate changes over the Common Era. *Paleoceanogr. Paleoclimatol.* **36**, e2020PA003934 (2021).

79. C. J. Willmott, K. Matsuura, Terrestrial air temperature and precipitation: monthly and annual time series (1950–1999) (version 5.0.1) (2001). http://climate.geog.udel.edu/~climate/html_pages/download.html. Accessed 1 April 2019.

80. U. Schneider *et al.*, GPCC full data reanalysis version 6.0 at 0.5°: Monthly land-surface precipitation from rain-gauges built on GTS-based and historic data. https://opendata.dwd.de/climate_environment/GPCC/html/fulldata_v6_doi_download.html. Accessed 16 May 2019.

81. I. Harris, P. D. Jones, T. J. Osborn, D. H. Lister, Updated high-resolution grids of monthly climatic observations - the CRU TS3.10 Dataset. *Int. J. Climatol.* **34**, 623–642 (2014).

82. M. S. Lachniet, Climatic and environmental controls on speleothem oxygen-isotope values. *Quat. Sci. Rev.* **28**, 412–432 (2009).

83. U. von Grafenstein, H. Erlernkeuser, P. Trimborn, Oxygen and carbon isotopes in modern fresh-water ostracod valves: Assessing vital offsets and autecological effects of interest for palaeoclimate studies. *Palaeogeogr. Palaeoclimatol. Palaeoecol.* **148**, 133–152 (1999).

84. J. Haslett, A. Parnell, A simple monotone process with application to radiocarbon-dated depth chronologies. *J. R. Stat. Soc. Ser. C Appl. Stat.* **57**, 399–418 (2008).

85. L. Comas-Bru *et al.*, SISALv2: A comprehensive speleothem isotope database with multiple age–depth models. *Earth Syst. Sci. Data* **12**, 2579–2606 (2020).

86. K. Atsawawaranunt, S. Harrison, L. Comas-Bru, SISAL (Speleothem Isotopes Synthesis and AnaLysis Working Group) database version 1b (2019). https://researchdata.reading.ac.uk/189/. Accessed 24 January 2020.

87. P. J. Reimer *et al.*, The IntCal20 Northern Hemisphere Radiocarbon Age calibration curve (0–55 cal kBP). *Radiocarbon* **62**, 725–757 (2020).

88. M. E. Mann, Smoothing of climate time series revisited. *Geophys. Res. Lett.* **35**, L16708 (2008).